Nuclear Materials and Energy 18 (2019) 275–280

Contents lists available at ScienceDirect

Nuclear Materials and Energy

journal homepage: www.elsevier.com/locate/nme

On the ion and electron temperature recovery after the ELM-crash at ASDEX upgrade

M. Cavedon[*,a], R. Dux[a], T. Pütterich[a], E. Viezzer[b], E. Wolfrum[a], M. Dunne[a], E. Fable[a], R. Fischer[a], G.F. Harrer[c], F.M. Laggner[d], A.F. Mink[a,e], U. Plank[a], U. Stroth[a,e], M. Willensdorfer[a], ASDEX Upgrade Team[f]

[a] Max Planck Institute for Plasma Physics, Boltzmannstr. 2, Garching 85748, Germany
[b] Dept. of Atomic, Molecular and Nuclear Physics, University of Seville, Seville 41012, Spain
[c] Institute of Applied Physics, TU Wien, Fusion@ÖAW, 1040, Vienna, Austria
[d] Princeton University, Princeton, NJ 08544, United States
[e] Physik-Department E28, Technische Universität München, Garching 85748, Germany
[f] see the author list "A. Kallenbach et al. Nucl. Fusion 57, 102015 (2017)"

ARTICLE INFO

Keywords:
ELM
Ion temperature
ETG
Neutral ionization
Fast Charge Exchange

ABSTRACT

The access to fast measurements, i.e. $\Delta t \approx 100$ μs, of the ions and the electrons during an entire edge localized cycle (ELM) reveals asymmetries in the recovery of the maximum edge gradients. Different magnetic fluctuations are found to correlate with the saturation of the edge ion temperature (T_i), electrons temperature (T_e) and density (n_e) gradients. In particular, while ∇T_i and ∇n_e clamp roughly 3.0 ms after the ELM-crash together with the onset of mid-frequency ($f \lesssim 50$ kHz) magnetic fluctuations, ∇T_e recovers to the pre-ELM conditions only after 7.0 ms and saturates with the appearance of high frequency fluctuations ($f \approx 200$ kHz). The effect of electron temperature gradient modes (ETGs) and of energy losses induced by ionization of neutrals are discussed as possible reasons for the delayed recovery of ∇T_e. The onset and the suppression of ETGs qualitatively follow the requirements of an increased electron heat transport. However, gyro-kinetic simulations are necessary to quantify the impact of ETGs. On the other hand, the impact of the neutral ionization during the density build-up as an electron energy loss channel is measured to be small compared to the total electron energy. The dominant terms in the electron energy balance are instead the radiative power and the ion-electron heat exchange.

1. Introduction

The fusion performance of any future reactor is closely related to the pressure at the top of the pedestal [1]. In the high confinement mode (H-mode), however, the edge localized mode (ELM) limits the growth of the pedestal by periodic relaxations of the steep gradient at the edge of the plasma. Moreover, the energy and particle fluxes flushed to the plasma facing components during ELMs pose one of the most serious technical challenges for future devices. For these reasons, ELMs have been an active subject of research since the discovery of the H-mode [2].

While the peeling-ballooning theory is successfully employed to describe the stability limit of the pedestal [3], the prediction of the evolution of the pedestal shape (height and width) inbetween ELMs, the so-called inter-ELM phase, needs additional constraints. Gyro-kinetic simulations indicate that the pre-ELM pedestal conditions are unstable with respect to several micro-instabilities of which micro tearing modes (MTMs) and kinetic ballooning modes (KBMs) are the dominant instabilities [4–6]. The onset of the latter is employed to limit the maximum achievable pressure gradient in the EPED model [7]. However, in the inter-ELM profile recovery other instabilities come into play, such as electron temperature gradient (ETG) modes and trapped electron modes (TEM) [8].

Several tokamaks reported on the rise of density and magnetic fluctuations during the pedestal recovery [9–12]. Their high frequency component correlates with the clamping of the maximum electron pressure gradient suggesting a KBM nature [10]. However, their existence at the high field side indicates a non-ballooning behavior [11]. At the same time, a good agreement is found by comparing experimentally determined toroidal mode numbers and non-linear MHD simulations during the ELM crash [13]. Distinct phases in the impurity transport have been already identified by means of fast charge

* Corresponding author.
E-mail address: marco.cavedon@ipp.mpg.de (M. Cavedon).

https://doi.org/10.1016/j.nme.2018.12.034
Received 9 August 2018; Received in revised form 29 December 2018; Accepted 30 December 2018
Available online 17 January 2019
2352-1791/ © 2019 The Authors. Published by Elsevier Ltd. This is an open access article under the CC BY-NC-ND license (http://creativecommons.org/licenses/BY-NC-ND/4.0/).

exchange (CX) measurements on fully-ionized carbon ($\Delta t < 300\mu s$): a rapid convective transport together with an increased energy diffusion have been found suggesting that the ELM-induced transport cannot be described by linear peeling-ballooning MHD [14,15]. In addition, a first insight on the ions and the radial electric field (E_r) during an ELM-cycle showed a fast recovery of the $E \times B$ velocity after the ELM-crash [14,15], also confirmed by CX-measurements on helium [16]. Furthermore, an asymmetry between ions and electrons has been found during the inter-ELM phase: while ∇T_i recovers on the same time scales as ∇n_e, ∇T_e takes longer to be back at the pre-ELM values [16].

In this work, the studies in [15] and [16] could be extended to different impurity species (boron and nitrogen) with a focus on the ELM recovery. Comparison to magnetic probe measurements shows a correlation between the profile behavior of ions and electrons and the onset of magnetic fluctuations (see Section 2). Furthermore, two hypotheses are discussed for the delayed recovery of the electron temperature gradient ∇T_e compared to the electron density ∇n_e and the ion temperature gradient ∇T_i [16,17]. To this end, interpretative transport simulations are designed to quantify the energy sources and sinks during the ELM-recovery (Section 3). Finally, the conclusions and the outlook are given in Section 4.

2. Correlating the recovery of the ion and electron profiles to magnetic fluctuations

ELM-resolved electron temperature and density profiles are routinely measured in several machines [9,17–19], while information on the ion and flow profiles are often not accessible. Recent developments of fast CX systems allow sub-ms measurements of the edge ion temperature, impurity flows and, via the radial force balance equations, of the $\mathbf{E} \times \mathbf{B}$ velocity, $v_{E \times B}$ [20,21]. These are of particular interest given the connection between $v_{E \times B}$ and the pedestal formation [22] and of the T_i/T_e ratio on the pedestal stability [23]. ELM-resolved ion and electron temperature measurements revealed asymmetries between the *e*- and *i*-channels during the ELM-crash and the recovery [16]. At the ELM-crash, the ion temperature in the vicinity of the separatrix increases such that $T_i/T_e \approx 5$ [15] indicating that the parallel ion heat transport is not negligible and can be comparable to that of the electrons in the SOL [24]. Note that recent developments of main ion CX-measurements at DIII-D show that $T_{i,D} < T_{i,C}$, leading to $T_{i,D}/T_e$ of approximately 2 at $\rho = 1$ for inter-ELM conditions [25]. Such a difference between the main and the impurity ion temperatures is not expected for typical AUG H-mode discharges since the energy equilibration time τ is shorter than the typical particle transport time at the edge of the plasma [26]. On the other hand, τ between deuterium ions is of the order of hundreds of μs, during events such as the ELM-crash it might not be possible to define an ion temperature at all. Ions which are possibly not equilibrated, however, do not influence the ion temperature measurements during the profile recovery because here typical timescales are of the order of milli-seconds. This is consistent with the observation from both main ion [27] and impurity CX [16] measurements that the recovery of ∇T_i after the ELM-crash appears to be faster than the one of ∇T_e and on the same time scale as ∇n_e. The delay of ∇T_e is unexpected since the H-mode transport barrier is a particle and heat transport barrier. However, the electron temperature gradient behaves differently indicating that the electron heat transport might be different or that local power losses might affect the recovery. Finally, the radial electric field $E_r = v_{E \times B} \cdot B$ drops to typical L-mode like values at the ELM-crash and it recovers to the pre-ELM conditions on the same time scales as ∇n_e and ∇T_i.

Comparing the ion and electron profiles to the magnetic data reveals a correlation between the evolution of the ion and electron gradients and the onset of magnetic fluctuations. Several discharges were designed to obtain detailed profiles at the edge of the plasma at the lowest ELM frequency possible to better separate the recovery phases. This has been achieved with high triangularity discharges, at a toroidal field of

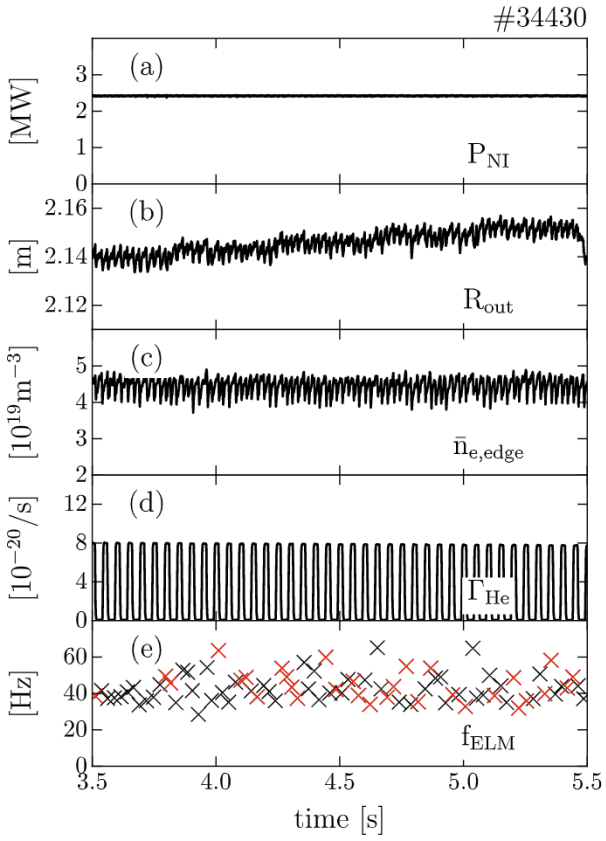

Fig. 1. Timetraces of a reference discharge: (a) neutral beam input power, (b) outer midplane plasma position, (c) line average edge density, (d) helium seeding rate, (e) ELM frequency (the red crosses indicate the ELM selected for the synchronization). (For interpretation of the references to colour in this figure legend, the reader is referred to the web version of this article.)

−2.5 T, plasma current of 0.8 MA and with an input power just above the L-H power threshold but sufficient for type-I ELMs [28]. Fig. 1 shows the time traces of the total neutral beam input power P_{NI} (a), the outer midplane plasma position R_{out} (b), the line average density $n_{e,edge}$ (c), the applied helium gas puff Γ_{He} (d), and the ELM frequency f_{ELM} (e) for the reference discharge. The helium puffs are necessary to increase the signal to noise ratio for the fast CX measurements, e.g. at a time resolution of 100μs. A plasma phase has been selected for the analysis in which the input power and density are constant (Fig. 1a and c). During this time window, the plasma has been swept radially to increase the radial coverage of the edge diagnostics (Fig. 1b). The resulting ELM frequency is about 40 Hz (Fig. 1d) which offers long inter-ELM phases, ideal for the analysis of the profile recovery. In Fig. 1d the red crosses indicate the 31 ELMs out of 80 ELMs used for the following analysis. The selection criteria is based on a rolling correlation like algorithm using the divertor shunt current signal I_{div}. The I_{div} signature of one reference ELM, chosen by its long inter-ELM phase without smaller ELMs, is step-wise correlated with the windowed I_{div}signal. In this way, a time-dependent correlation of the reference ELM with the other ELMs can be obtained where the value of the local maximum indicates the closeness while the time of the occurrence the synchronization time point. An arbitrary threshold on the correlation of 0.98 has been used to assure similarity in both the ELM-peak characteristics and the inter-ELM phase. The synchronized I_{div} is shown in Fig. 2g. Note that the synchronization procedure introduces scatter which depends on the specific temporal resolution of a signal. In this work, the electron and ion diagnostics are sampled at a time resolution of 100μs which results in an uncertainty of 300 μs due to possible mis-synchronization of a single frame. To avoid confusion, all the measurements presented later are re-binned to this time resolution. Note that the electron profile

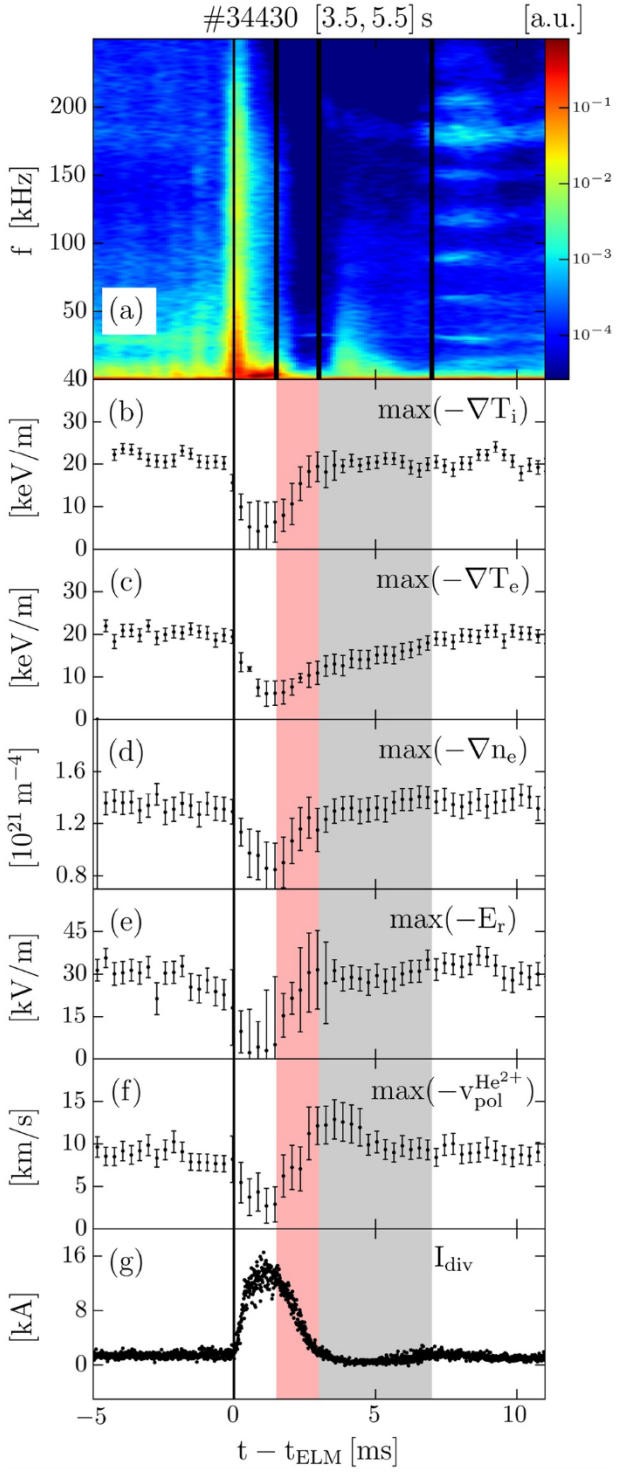

Fig. 2. Comparison of the magnetic fluctuations with the profile gradient recovery (all the signals are ELM-synchronized): (a) Spectrogram of an outer midplane $\dot{B}_r$ pick-up-coil, (b) $\max(-\nabla T_i)$, (c) $\max(-\nabla T_e)$, (d) $\max(-\nabla n_e)$, (e) $\max(-E_r)$, (f) $\max(-v_{pol}^{He^{2+}})$, and (g) I_{div}. The red shaded region highlights the fast recovery of $\max(-\nabla T_i)$, $\max(-\nabla n_e)$ and $\max(-E_r)$ while the gray one the longer time scales of the $\max(-\nabla T_e)$ recovery. (For interpretation of the references to colour in this figure legend, the reader is referred to the web version of this article.)

data at 100μs resolution during the entire ELM-cycle has been obtained following the procedure described in [16].

Following the analysis procedure described in [16], the ELM-synchronized maximum gradients of T_i, T_e and n_e are shown in Figs. 2b–d, respectively. Moreover, the minimum of the radial electric field, determined from the radial force balance for He^{2+}, is presented in Fig. 2e and the minimum of the poloidal velocity of the fully ionized helium $v_{pol}^{He^{2+}}$ is shown in Fig. 2f. Here, negative poloidal velocities, as well as a negative E_r, are in the electron diamagnetic drift direction. In Fig. 2e and f, the maximum of the negative E_r and $v_{pol}^{He^{2+}}$ are shown to highlight the large reduction, in absolute value, of both quantities at the ELM-crash. The divertor shunt current I_{div} is used as a reference signal for the synchronization (Fig. 2g). The profile gradients are compared to the ELM-synchronized spectrogram from a pick-up coil measuring the radial fluctuations of the magnetic field $\dot{B}_r$ and placed at the outer midplane (Fig. 2a). The spectrogram shows the typical pattern as described in [11,13]: at the ELM crash a strong broadband magnetic activity is observed ($t \in [0, 1.5]$ ms) followed by a quiet phase ($t \in [1.5, 3.0]$ ms). Between roughly 3.0 and 7.0 ms magnetic activity with frequency up to 50 kHz re-appears. This is then replaced, after 7 ms, by fluctuations with dominant frequency around 180 kHz and several other distinct frequencies. The high frequency magnetic fluctuations can get weaker before the ELM ($t < 0$ms) as already observed in [13]. Note that the quiet phase between 1.5 and 3.0 ms coincides with the recovery of ∇T_i, ∇n_e and E_r (see red shaded area) to the pre-ELM values while the reestablishment of ∇T_e lasts until the onset of the high frequency fluctuations at $t = 7$ ms (see gray shaded area). According to the relation presented in [11], the pre-ELM value of the edge radial electric field (≈ -30kV/m, Fig. 2e) is consistent with the dominant magnetic fluctuation frequency of 180 kHz suggesting that the observed modes have the same nature.

The minimum of the He^{2+} poloidal velocity (Fig. 2e) is first decreased by the ELM, then recovers and becomes even larger than the pre-ELM value for a short time. This has been observed before in [16]. Note that the poloidal velocity of a plasma species α is a critical contribution in the radial force balance since it is multiplied by the toroidal field B_{tor}:

$$E_r = \frac{\nabla_r (n_\alpha T_\alpha)}{e Z_\alpha n_\alpha} + v_{tor,\alpha} B_{pol} - v_{pol,\alpha} B_{tor} \quad (1)$$

In the edge of ASDEX Upgrade (AUG) the toroidal velocity $v_{tor,\alpha}$ is small [29], therefore $v_{pol,\alpha}$ is the dominant contribution for medium- to high-Z species because the diamagnetic term, i.e. the first term in the Eq. (1), is divided by the charge Z_α. In the case of He^{2+}, both the diamagnetic and the poloidal velocity contribution are important for the determination of E_r. Therefore, the spin-up in $v_{pol,\alpha}$ is not necessarily reflected in the reconstruction of E_r. In Fig. 3, the ELM-synchronized poloidal velocity of He^{2+} (a), B^{5+} (b) and N^{7+} (c) are compared. The poloidal velocity of B^{5+} and of N^{7+} do not exhibit the same spin-up as $v_{pol}^{He^{2+}}$, consistent with the E_r measurements because for $Z_\alpha = 5, 7$, E_r is approximately $-v_{pol,\alpha} B_{tor}$. However, the measurements of the different poloidal velocities are obtained in different conditions and time resolutions. Namely, the use of nitrogen seeding increases f_{ELM} [30,31] and hence a match of the ELM-cycle duration with the reference case was not possible. Furthermore, fast CX measurements, i.e. $\Delta t \approx 100\mu s$, were only possible in discharges with He and N seeding while an exposure time of 2.3 ms has been employed when measuring boron. This is because external seeding of B_2H_6 at the time and the intrinsic B leads to a limited signal.

The asymmetry in the time scales of the ELM-recovery of the ion and electron maximum temperature gradients has been first observed in [16] and confirmed in [27] by means of main ion CX measurements. Note that this also implies a good thermalization of the impurity. On the other hand, the different behavior of electrons and ions is puzzling. The delay in the recovery of ∇T_e must be due to either an enhanced electron heat transport, an additional energy loss or a combination of both. In particular, the possible effect of electron temperature gradient modes (ETGs) as electron heat transport mechanism or the effect of neutrals as energy loss are discussed in the next section.

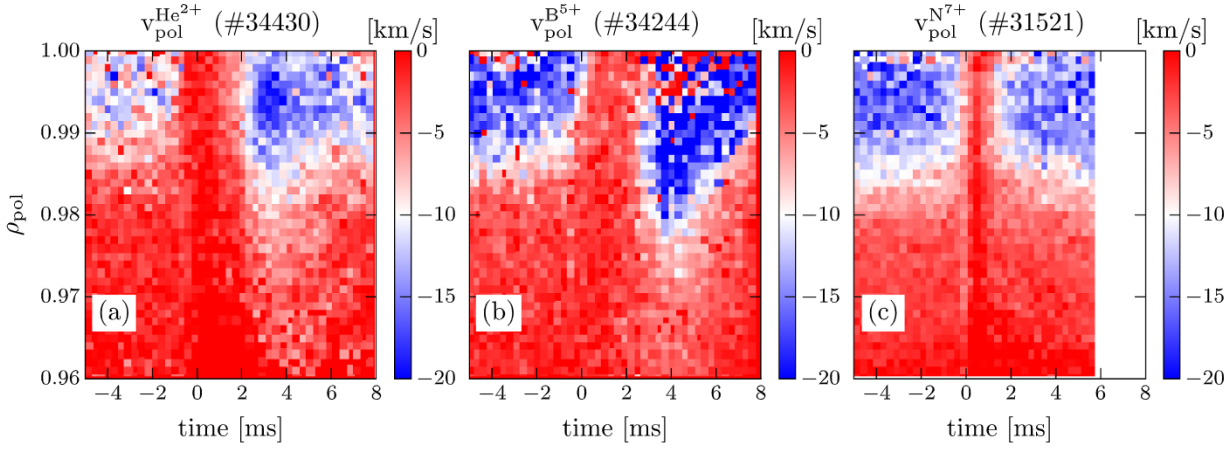

Fig. 3. ELM-synchronized poloidal velocity profiles of He^{2+} (a), B^{5+} (b) and N^{7+} (c). Note that the data are taken in different discharges with different seeding conditions and ELM frequencies. (For interpretation of the references to colour in this figure legend, the reader is referred to the web version of this article.)

3. On the delayed recovery of the electron temperature gradient

In this section, two possible mechanisms for the delayed recovery of ∇T_e are examined: electron temperature gradient modes (ETGs), and the ionization of neutrals.

3.1. Electron temperature gradient modes

Electron temperature gradient modes are electrostatic instabilities which induce radial electron heat losses and hence are a possible candidate for the enhanced transport. A critical gradient formula for the destabilization of the ETG has been derived from gyro-kinetic simulations in the core [32] and was extended to the edge [6]. If $R/L_{T_e} > (R/L_{T_e})_{crit}$ then ETGs are destabilized, where $(R/L_{T_e})_{crit}$ is

$$(R/L_{T_e})_{crit} = \max\begin{cases} A = (1+\tau)(1.33 + 1.91\hat{s}/q)\cdot \\ \quad (1 - 1.5\epsilon)[1 + 0.3\epsilon(d\kappa/d\epsilon)] \\ B = 1.2\cdot R/L_{n_e} \end{cases} \quad (2)$$

and $\tau = (1 + Z_{eff}\, T_e/T_i)$, $\hat{s}$ is the magnetic shear, q is the safety factor, ϵ is the inverse aspect ratio, and κ is the elongation of the magnetic surface. In Fig. 4a the profiles of A and B (see Eq. (2)) are shown. Given the strong ∇n_e present at the edge, the term B is largely dominating the ETG stabilization as already pointed out in [6]. This is the case also if $T_e \approx T_i$. Hence, by comparing R/L_{T_e} (black) and $(R/L_{T_e})_{crit} \approx 1.2\cdot R/L_{n_e}$ (green) in Fig. 4b at $\rho_{pol} = 0.993$, i.e. in the steep gradient region, the existence of ETGs can be judged. Right after the ELM-crash until roughly 2.5 ms, $R/L_{T_e} > (R/L_{T_e})_{crit}$ suggesting that ETGs could be active in this phase. After that, due to the recovery of ∇n_e, $R/L_{T_e} \approx (R/L_{T_e})_{crit}$ which indicates that the ETGs might be suppressed. Note that the possible presence of ETGs in this phase is consistent with the reduced activity in the magnetics (see Fig. 2a). However, while the ETG activity is roughly consistent with the observation of additional transport delaying the recovery of ∇T_e, ETGs should extend longer than $\approx$ 2.5ms to reproduce the evolution in Fig. 2 in which ∇T_e is fully recovered only 7 ms after the ELM-crash. On the other hand, Eq. (2) gives only an indication of the relative strength of the ETGs since their onset is smooth and the formula (2) only considers the linear instability threshold [6,33,34]. Therefore, no quantitative estimation can be extracted from Fig. 4. Note that since $A < B$, the stabilization of ETG is determined by $\eta_e = R/L_{n_e}/R/L_{T_e}$. Hence, large uncertainties are involved in the calculation of the ETG stabilization and it might be that they are still present when ∇T_e is close to $(R/L_{T_e})_{crit}$. Finally, to relate the enhanced electron heat transport to the ETGs, a quantitative estimation of their effect compared to the other micro-instabilities and to non-linear MHD transport is necessary. To access this point, dedicated gyro-kinetic simulations including data from ions and electrons and non-linear MHD-modelling are ongoing.

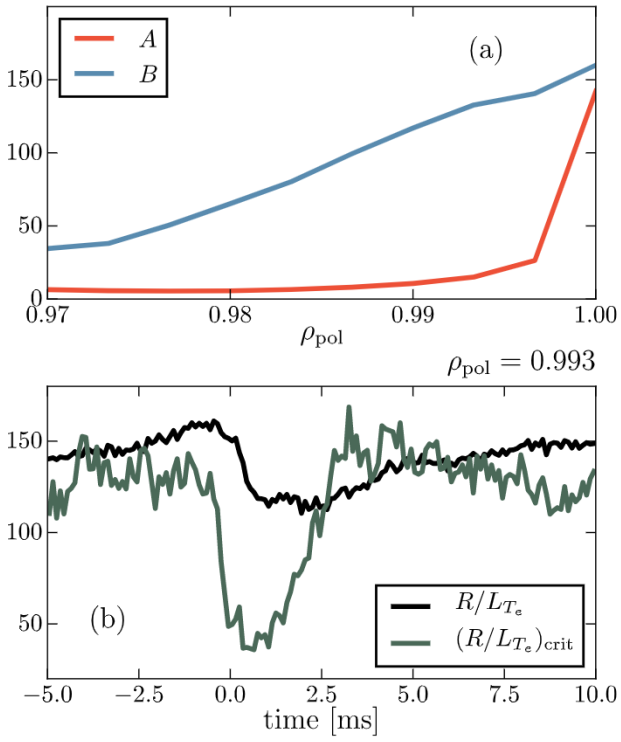

Fig. 4. (a): Pre-ELM ($-4ms < t < -2ms$) edge profile of the $(R/L_{T_e})_{crit}$ terms in equation (2). (b): Evolution of R/L_{T_e} (black) and $(R/L_{T_e})_{crit}$ (green) during an ELM cycle at $\rho_{pol} = 0.993$. (For interpretation of the references to colour in this figure legend, the reader is referred to the web version of this article.)

3.2. Neutral ionization

Another possible mechanism which could delay the recovery of ∇T_e is the energy lost in the ionization of the neutrals. Due to the strong density build up in the initial ELM-recovery phase, a large amount of neutrals needs to be ionized. To compare this loss channel to the other energy sinks and sources, transport simulations have been performed using the 1.5D transport code ASTRA [35,36]. The analysis of the electron heat transport channel is presented in the following section.

Transport simulations generally solve a system of 1D diffusion equations, similar to the one derived in [37], for densities and

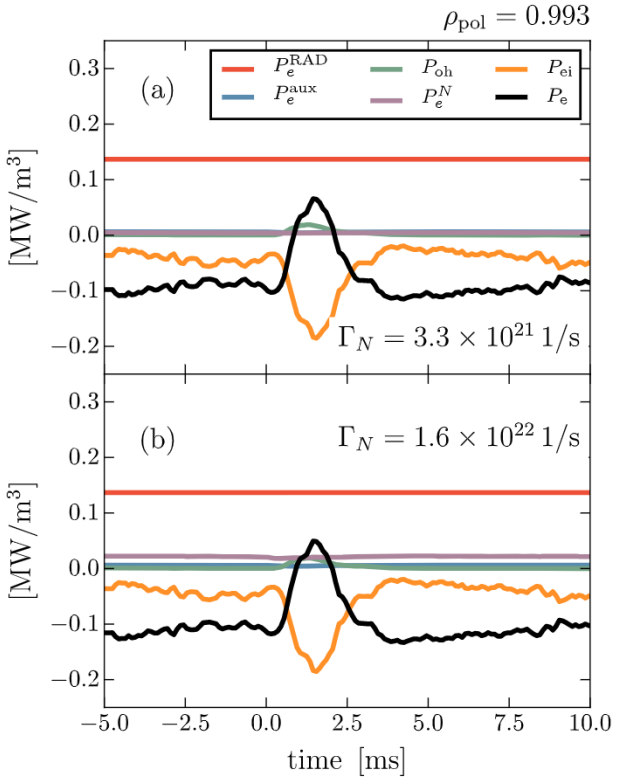

Fig. 5. Modelled electron energy components during the ELM-recovery as defined in equations (3) at $\rho_{\rm pol} = 0.993$ for respectively $\Gamma_N = 3.3 \times 10^{21}$ atoms/s (a) and $\Gamma_N = 1.6 \times 10^{22}$ atoms/s (b). (For interpretation of the references to colour in this figure legend, the reader is referred to the web version of this article.)

temperatures of different plasma species. A variety of other modules are used to describe, for instance, auxiliary heating, MHD stability, current drive etc. Here, the neutral module of ASTRA is used to measure the loss of electron energy due to atomic processes during the ELM-recovery. This module cannot distinguish between wall-recycling and gas puff. Neutrals are modelled as an effective source (or influx) Γ_N, most likely dominated by recycling at the edge [38,39], with a certain energy E_N. By giving as input the measured density and temperature profiles together with Γ_N, radiative power and auxiliary heating power, it is possible to determine the sources and sinks of the ion P_i and electron P_e energies. These are defined as follows:

$$P_e = P_{\rm oh} + P_e^{\rm aux} - P_{ei} - P_e^{\rm RAD} - P_e^N \quad (3)$$

$$P_i = P_i^{\rm aux} + P_{ei} - P_i^N \quad (4)$$

where $P_{\rm oh}$ is the ohmic power, $P_e^{\rm aux}$ and $P_i^{\rm aux}$ is the auxiliary ion and electron heating, P_{ei} is the electron-ion heat exchange, $P_e^{\rm RAD}$ is the power lost for radiation, P_e^N and P_i^N are the sum of the losses due to atomic processes (ionization, recombination, and charge exchange for the ions). By comparing P_e^N with the total P_e, the relative impact of atomic processes on the electron energy can be determined thus giving an idea if such losses could potentially affect the recovery of ∇T_e. However, since the neutral fluxes are basically unknown within roughly two orders of magnitude ($\Gamma_N \approx 10^{20} - 10^{22}$atoms/s) [40,41], a scan in Γ_N needs to be performed which, for simplicity, has been kept constant during the ELM-recovery. Furthermore, the particle convection v at the plasma edge has been set to zero and only cold neutrals are considered at the energy of dissociated Franck–Condon neutrals of roughly 2.5 eV. A more consistent approach would be to perform predictive simulations of n_e by imposing different sets of particle diffusion coefficient D, Γ_N and v, similarly to what was done in [40]. The interpretative simulations have been carried out on the discharge analyzed in [16] which had higher input power (5 MW) and consequently higher ELM-frequency ($f \approx 80$Hz) compared to the one shown in Section 2.

Fig. 5a and b show the single terms in Eq. (3) at $\rho_{\rm pol} = 0.993$ for respectively $\Gamma_N = 3.3 \times 10^{21}$atoms/s and 1.6×10^{22} atoms/s. In the case of $\Gamma_N = 3.3 \times 10^{21}$atoms/s (Fig. 5a) P_e^N (violet) is roughly a factor 50 smaller than P_e (black) and hence negligible. Since $P_e^N \sim \Gamma_N$, even by going to the extreme case of $\Gamma_N = 1.6 \times 10^{22}$ atoms/s, the energy losses due to atomic processes remain too small to really affect the electron energy balance. Note that the ohmic (green) and the auxiliary (blue) heating contributions are also very small at these radial positions. On the other hand, the energy exchange between electrons and ions P_{ei} (orange) is the dominating term of P_e together with the radiation (red). Note that P_{ei} is proportional to $T_e - T_i$ and if $T_e \approx T_i$, obviously, the energy exchange goes to zero. However, for the case analyzed here the pre-ELM $T_{\rm He^{2+}}/T_e(\rho_{\rm pol} = 0.993) \approx 2$ [16], hence $P_{ei} \neq 0$, which is consistent with the values obtained at DIII-D by means of main ion CX measurements [25]. $P_e^{\rm RAD}$ is kept constant during the entire ELM-cycle because an ELM-synchronized deconvolution of the bolometer measurements was too uncertain to be used. Note that the local pedestal $P_e^{\rm RAD}$ might not increase a lot during the ELM-crash since the density drops and the impurities are flushed out of the confined region. P_{ei}, instead, peaks right after the ELM-crash when, close to the separatrix, $T_i \gg T_e$. After that, T_i gets close to T_e and slightly rises until the next ELM crash [16] and so does P_{ei} since T_e stays roughly constant at the separatrix. Note that P_{ei} enters in the electron energy balance (Eq. (3)) with a negative sign and if $T_i > T_e$, as in this case, P_{ei} positively contributes to the total electron energy. The trend of P_{ei} after the ELM-crash is reminiscent of the recovery of ∇T_e and might be one of the key parameters to understand the asymmetry between ion and electron temperature recovery. Note that, however, the local sinks and sources at the edge are much smaller than the energy flux arriving from the core plasma. Hence, the local dynamics might be strongly influenced by the transport further inside the plasma.

4. Summary and outlook

Sub-ms measurements of the ion temperature and the impurity flows reveal a different time scale for the recovery of the maximum gradient of the ion and electron temperatures. The maximum of ∇T_i and of ∇n_e saturate roughly 3 ms after the ELM-crash together with the onset of mid frequency magnetic fluctuations ($f < 50$ kHz) while ∇T_e is recovered to the pre-ELM values only after 7.0 ms simultaneously with the establishment of high frequency fluctuations ($f = 180$ kHz). Transport simulations show that the local energy sink due to atomic processes is negligible compared to the radiation loss and the ion-electron coupling. The trend of the latter resembles the recovery of ∇T_e while ELM-resolved radiation profiles might be possible in the future. Finally, the destabilization of the electron temperature gradient modes is shown to qualitatively describe the enhanced electron energy transport required for delaying the recovery of ∇T_e. However, a quantitative estimation of ETGs impact on the total heat transport requires dedicated gyro-kinetic simulations.

Acknowledgements

The authors gratefully acknowledge C. Angioni and D. Told for their help and advice regarding the electron temperature gradient mode physics.

References

[1] E.J. Doyle, et al., Chapter 2: plasma confinement and transport, Nucl. Fusion 47 (6) (2007) S18. URL: http://stacks.iop.org/0029-5515/47/i=6/a=S02
[2] H. Zohm, Edge localized modes (elms), Plasma Phys. Controll. Fusion 38 (2) (1996) 105. URL: http://stacks.iop.org/0741-3335/38/i=2/a=001
[3] P.B. Snyder, et al., Edge localized modes and the pedestal: a model based on coupled peelingballooning modes, Phys. Plasmas 9 (5) (2002) 2037–2043, https://doi.

org/10.1063/1.1449463.
[4] D. Dickinson, et al., Towards the construction of a model to describe the inter-elm evolution of the pedestal on mast, Plasma Phys. Controll. Fusion 53 (11) (2011) 115010. URL: http://stacks.iop.org/0741-3335/53/i=11/a=115010
[5] S. Saarelma, et al., Mhd and gyro-kinetic stability of jet pedestals, Nucl. Fusion 53 (12) (2013) 123012. URL: http://stacks.iop.org/0029-5515/53/i=12/a=123012
[6] D. Told, et al., Gyrokinetic microinstabilities in asdex upgrade edge plasmas, Phys. Plasmas 15 (10) (2008) 102306, https://doi.org/10.1063/1.3000132.
[7] P. Snyder, et al., A first-principles predictive model of the pedestal height and width: development, testing and iter optimization with the eped model, Nucl. Fusion 51 (10) (2011) 103016. URL: http://stacks.iop.org/0029-5515/51/i=10/a=103016
[8] D. Hatch, et al., Gyrokinetic study of asdex upgrade inter-elm pedestal profile evolution, Nucl. Fusion 55 (6) (2015) 063028. URL: http://stacks.iop.org/0029-5515/55/i=6/a=063028
[9] R.J. Groebner, et al., Temporal evolution of h-mode pedestal in DIII-D, Nucl. Fusion 49 (4) (2009) 045013. URL: http://stacks.iop.org/0029-5515/49/i=4/a=045013
[10] A. Diallo, et al., Observation of edge instability limiting the pedestal growth in tokamak plasmas, Phys. Rev. Lett. 112 (2014) 115001, https://doi.org/10.1103/PhysRevLett.112.115001.
[11] F.M. Laggner, et al., High frequency magnetic fluctuations correlated with the inter-elm pedestal evolution in asdex upgrade, Plasma Phys. Controll. Fusion 58 (6) (2016) 065005. URL: http://stacks.iop.org/0741-3335/58/i=6/a=065005
[12] A. Diallo, et al., Correlations between quasi-coherent fluctuations and the pedestal evolution during the inter-edge localized modes phase on diii-d, Phys. Plasmas 22 (5) (2015) 056111, https://doi.org/10.1063/1.4921148.
[13] F. Mink, et al., Toroidal mode number determination of elm associated phenomena on asdex upgrade, Plasma Phys. Controll. Fusion 58 (12) (2016) 125013.
[14] M.R. Wade, et al., Edge-localized-mode–induced transport of impurity density, energy, and momentum, Phys. Rev. Lett. 94 (2005) 225001, https://doi.org/10.1103/PhysRevLett.94.225001.
[15] M.R. Wade, et al., Edge impurity dynamics during an edge-localized mode cycle on DIII-D, Phys. Plasmas 12 (5) (2005) 056120, https://doi.org/10.1063/1.1891745.
[16] M. Cavedon, et al., Pedestal and e r profile evolution during an edge localized mode cycle at asdex upgrade, Plasma Phys. Controll. Fusion 59 (10) (2017) 105007. URL: http://stacks.iop.org/0741-3335/59/i=10/a=105007
[17] A. Burckhart, et al., Inter-ELM behaviour of the electron density and temperature pedestal in ASDEX upgrade, Plasma Phys. Controll. Fusion 52 (10) (2010) 105010. URL: http://stacks.iop.org/0741-3335/52/i=10/a=105010
[18] R. Behn, et al., Edge profiles of electron temperature and density during ELMy h-mode in ohmically heated TCV plasmas, Plasma Phys. Controll. Fusion 49 (8) (2007) 1289. URL: http://stacks.iop.org/0741-3335/49/i=8/a=013
[19] M.N.A. Beurskens, et al., Pedestal and scrape-off layer dynamics in ELMy h-mode plasmas in JET, Nucl. Fusion 49 (12) (2009) 125006. URL: http://stacks.iop.org/0029-5515/49/i=12/a=125006
[20] K.H. Burrell, et al., Improved charge-coupled device detectors for high-speed, charge exchange spectroscopy studies on the diii-d tokamak, Rev. Sci. Instrum. 75 (10) (2004) 3455–3457, https://doi.org/10.1063/1.1787949.
[21] M. Cavedon, et al., A fast edge charge exchange recombination spectroscopy system at the asdex upgrade tokamak, Rev. Sci. Instrum. 88 (4) (2017) 043103, https://doi.org/10.1063/1.4979801.
[22] H. Biglari, et al., Influence of sheared poloidal rotation on edge turbulence, Phys. Fluids B 2 (1) (1990) 1, https://doi.org/10.1063/1.859529.
[23] P.B. Snyder, et al., Characterization of peelingballooning stability limits on the pedestal, Plasma Phys. Controll. Fusion 46 (5A) (2004) A131. URL: http://stacks.iop.org/0741-3335/46/i=5A/a=014
[24] D. Carralero, et al., Recent progress towards a quantitative description of filamentary sol transport, Nucl. Fusion 57 (5) (2017) 056044. URL: http://stacks.iop.org/0029-5515/57/i=5/a=056044
[25] S.R. Haskey, et al., Main ion and impurity edge profile evolution across the l- to h-mode transition on diii-d, Plasma Phys. Controll. Fusion 60 (10) (2018) 105001. URL: http://stacks.iop.org/0741-3335/60/i=10/a=105001
[26] E. Viezzer, et al., High-accuracy characterization of the edge radial electric field at asdex upgrade, Nucl. Fusion 53 (5) (2013) 053005. URL: http://stacks.iop.org/0029-5515/53/i=5/a=053005
[27] F.M. Laggner, et al., Pedestal structure and inter-elm evolution for different main ion species in asdex upgrade, Phys. Plasmas 24 (5) (2017) 056105, https://doi.org/10.1063/1.4977461.
[28] W. Kerner, et al., The scaling of the giant elm frequency, Nucl. Fusion 37 (4) (1997) 493. URL: http://stacks.iop.org/0029-5515/37/i=4/a=I07
[29] E. Viezzer, et al., Collisionality dependence of edge rotation and inout impurity asymmetries in asdex upgrade h-mode plasmas, Nucl. Fusion 55 (12) (2015) 123002. URL: http://stacks.iop.org/0029-5515/55/i=12/a=123002
[30] P.A. Schneider, et al., Pedestal and edge localized mode characteristics with different first wall materials and nitrogen seeding in asdex upgrade, Plasma Phys. Controll. Fusion 57 (1) (2015) 014029. URL: http://stacks.iop.org/0741-3335/57/i=1/a=014029
[31] L. Frassinetti, et al., Elm behavior in asdex upgrade with and without nitrogen seeding, Nucl. Fusion 57 (2) (2017) 022004. URL: http://stacks.iop.org/0029-5515/57/i=2/a=022004
[32] F. Jenko, et al., Critical gradient formula for toroidal electron temperature gradient modes, Phys. Plasmas 8 (9) (2001) 4096–4104, https://doi.org/10.1063/1.1391261.
[33] W. Horton, Drift waves and transport, Rev. Mod. Phys. 71 (1999) 735–778, https://doi.org/10.1103/RevModPhys.71.735.
[34] F. Jenko, et al., Gyrokinetic turbulence under near-separatrix or nonaxisymmetric conditions, Phys. Plasmas 16 (5) (2009) 055901, https://doi.org/10.1063/1.3089603.
[35] G.V. Pereverzev, et al., ASTRA - Automated System for TRansport Analysis, Technical Report, IPP Report, 2002.
[36] E. Fable, et al., Novel free-boundary equilibrium and transport solver with theory-based models and its validation against asdex upgrade current ramp scenarios, Plasma Phys. Controll. Fusion 55 (12) (2013) 124028. URL: http://stacks.iop.org/0741-3335/55/i=12/a=124028
[37] F.L. Hinton, R.D. Hazeltine, Theory of plasma transport in toroidal confinement systems, Rev. Mod. Phys. 48 (1976) 239–308, https://doi.org/10.1103/RevModPhys.48.239.
[38] M. Wischmeier, et al., High recycling outer divertor regimes after type-i elms at high density in asdex upgrade, J. Nucl. Mater. 363–365 (2007) 448–452, https://doi.org/10.1016/j.jnucmat.2007.01.041. Plasma-Surface Interactions-17
[39] A.Y. Pigarov, et al., Multi-fluid transport code modeling of time-dependent recycling in elmy h-mode, Phys. Plasmas 21 (6) (2014) 062514, https://doi.org/10.1063/1.4885346.
[40] M. Willensdorfer, et al., Particle transport analysis of the density build-up after the lh transition in asdex upgrade, Nucl. Fusion 53 (9) (2013) 093020. URL: http://stacks.iop.org/0029-5515/53/i=9/a=093020
[41] F.M. Laggner, et al., Divertor, scrape-off layer and pedestal particle dynamics in the elm cycle on asdex upgrade, Plasma Phys. Controll. Fusion 60 (2) (2018) 025002. URL: http://stacks.iop.org/0741-3335/60/i=2/a=025002